2017

Roles of Free Electrons and H2O2 in the Optical Breakdown-Induced Photochemical Reduction of Aqueous [AuCl4]-

Victoria K. Meader
VCU

Mallory G. John
VCU

Collin Rodrigues
VCU

Katharine M. Tibbetts
VCU, kmtibbetts@vcu.edu

On the Roles of Free Electrons and H_2O_2 in the Optical Breakdown-Induced Photochemical Reduction of Aqueous $[AuCl_4]^-$

Victoria Kathryn Meader, Mallory G. John, Collin J. Rodrigues, and Katharine Moore Tibbetts[*]

Department of Chemistry, Virginia Commonwealth University, Richmond, VA 23284

E-mail: kmtibbetts@vcu.edu

Phone: (804)-828-7515

Abstract

Free electrons and H_2O_2 formed in an optical breakdown plasma are found to directly control the kinetics of $[AuCl_4]^-$ reduction to form Au nanoparticles (AuNPs) during femtosecond laser-assisted synthesis of AuNPs. The formation rates of both free electrons and H_2O_2 strongly depend on the energy and duration of the 800 nm laser pulses over the ranges of $10 - 2400$ μJ and $30 - 1500$ fs. By monitoring the conversion of $[AuCl_4]^-$ to AuNPs using *in situ* UV-vis spectroscopy during laser irradiation, the first- and second-order rate constants in the autocatalytic rate law, k_1 and k_2, were extracted and compared to the computed free electron densities and experimentally measured H_2O_2 formation rates. For laser pulse energies of 600 μJ and lower at all pulse durations, the first-order rate constant, k_1, was found to be directly proportional to the theoretically calculated plasma volume, in which the electron density exceeds the

threshold value of 1.8×10^{20} cm^{-3}. The second-order rate constant, k_2, was found to correlate with the measured H$_2$O$_2$ formation rate at all pulse energies and durations, resulting in the empirical relationship $k_2 \sim$ H$_2$O$_2{}^{0.5}$. We have demonstrated that the relative composition of free electrons and H$_2$O$_2$ in the optical breakdown plasma may be controlled by changing the pulse energy and duration, which may make it possible to tune the size and dispersity of AuNPs and other metal nanoparticle products synthesized with femtosecond laser-based methods.

1 Introduction

The interactions of intense, ultrashort laser pulses with condensed media give rise to nonlinear optical phenomena, enabling applications including: white light lasers,[1] remote optical sensing,[2,3] nanostructure writing onto solid surfaces,[4,5] and cellular nanosurgery.[6–8] The initial process of laser-energy deposition involves the generation of a localized, weakly ionized plasma,[8–12] which leads to supercontinuum emission (SCE), optical breakdown (OB) of the medium, or both.[13,14] SCE results in a significant broadening of the initial input spectrum, and propagation of the white light as filaments in the medium,[14,15] while OB produces a dense, opaque microplasma when a sufficiently high free-electron density is achieved.[8,12]

Intense femtosecond-laser deposition in aqueous media resulting in OB, SCE, or both, has recently been employed to drive the photochemical reduction of metal salt precursors to form metal nanoparticles.[16–27] This "green" approach to metal nanoparticle synthesis requires no added chemical reducing agents and can yield some degree of control over the size and shape of gold nanoparticles (AuNPs) without added surfactants or capping agents.[24–26] In these experiments, the primary role of water-photolysis through OB and SCE is to produce reactive species such as solvated electrons and H $\cdot$, which drive metal-salt reduction.[16–18,21,22,25,27] In particular, it has been proposed that the laser intensity, or irradiance, must be sufficiently high to produce SCE in order to achieve the requisite solvated-electron densities for photochemical reduction.[21] Additionally, OB and SCE in water generate both short- and long-lived

reactive oxygen species such as OH$\cdot$ and H_2O_2, respectively.[28] The formation of H_2O_2 has been shown to promote reduction of $[AuCl_4]^-$ to form AuNPs, even after laser irradiation is terminated,[22,24-26] while excessive H_2O_2 formation in OB plasmas was found to result in oxidation of silver nanoparticles to form Ag^+.[29]

To quantify the roles of solvated electrons and H_2O_2 in driving the photochemical reduction of $[AuCl_4]^-$ to form AuNPs, this work investigates the effects of the femtosecond-laser pulse energy and pulse duration on the reduction kinetics of $[AuCl_4]^-$. Of particular importance is to minimize the generation of white light filaments in the aqueous medium resulting from SCE,[13] which results in intensity-clamping that limits the concentration of reactive species in the focal region.[15,23] Filamentation in aqueous media can be limited by using a tight-focusing geometry with large numerical aperture,[13] simultaneous spatial- and temporal-focusing (SSTF),[30] or spatial beam shaping.[5,31] Both tight-focusing[17,20] and SSTF with pulse-stretching to 36 ps[22-26] have been used for this purpose in previous studies of femtosecond laser-induced reduction of $[AuCl_4]^-$. To allow for continuous variation of the pulse duration from $30-1500$ fs, this work uses a tight-focusing geometry to prevent filamentation.

The reduction kinetics of $[AuCl_4]^-$ to AuNPs follow an autocatalytic rate law upon both chemical reduction[32-34] and femtosecond-laser processing.[25,27] We will show that the first-order nucleation rate constant associated with this rate law is directly proportional to the volume of the OB microplasma predicted by calculations of the free-electron density, while the second-order autocatalytic growth rate constant is correlated to the rate of H_2O_2 production during irradiation of water. By varying both the pulse energy and duration over at least two orders of magnitude, we show that extensive control over the relative production of free electrons and H_2O_2 in OB microplasmas is possible, which may enable the future tailoring of the chemical composition of OB microplasmas for further applications in addition to metal nanoparticle synthesis.

2 Experimental Methods

2.1 Materials

Potassium tetrachloroaurate(III) (Strem Chemicals) was used as obtained, as were potassium hydroxide and HPLC-grade water (Fisher Scientific). A working solution containing 0.1 mM $KAuCl_4$ and 0.35 mM KOH was prepared for experimental runs from stock solutions of $KAuCl_4$ (25 mM) and KOH (500 mM), respectively. The working solution was prepared 18-24 hours before carrying out experimental runs and was stored at 6 °C. For each experiment, 3 mL of the working solution was transferred to a cuvette and allowed to equilibrate to room temperature. The working solution pH was measured to confirm that it was in the range of 5.3 ± 0.2.

2.2 Instrumentation

Laser irradiation was performed using a titanium-sapphire-based chirped-pulse amplifier (Astrella, Coherent, Inc.) delivering 7 mJ, 30 fs pulses with bandwidth centered at 800 nm at a 1 kHz repetition rate. The pulse energy was varied from $10 - 2400$ μJ with a zero-order $\lambda/2$ waveplate (ThorLabs, Inc.) and broadband thin-film polarizer (Altechna), as well as a dispersion compensated 90:10 (R:T) beamsplitter (Newport, Inc.) to reach pulse energies below 300 μJ. The linear chirp of the laser pulse was controlled by detuning the compressor grating from its zero-dispersion position to produce 200 fs (positive and negative chirp), 750 fs (negative chirp), and 1500 fs (negative chirp). All pulse durations were measured by Frequency Resolved Optical Gating[35] (Figure S1 in the Supporting Information).

The 11 mm ($1/e^2$) diameter beam out of the laser was expanded to a diameter $D = 29$ mm ($1/e^2$) prior to focusing with a $f = 50$ mm aspheric lens (Figure 1(a)). The resulting focusing geometry is $f/1.7$, which is similar to the tightest focusing condition with a microscope objective reported in ref[13] and is significantly tighter than other recently reported focusing geometries for Gaussian beams.[36,37] The beam waist and Rayleigh range in air were measured

with a CCD camera (ThorLabs, Inc.) to be $w_0 = 6.52\ \mu$m and $z_r = 77.7\ \mu$m, respectively (Supporting Information, Figure S2). The focusing conditions correspond to a geometric numerical aperture NA $= n \sin \arctan(D/2f) = 0.37$ in water and a Gaussian beam numerical aperture NA $= w_0/z_r = 0.084$. Based on the pulse energies and durations we used, the calculated peak irradiance at the focus (neglecting losses and plasma-induced defocusing in front of the focus[13,14,38]) ranges from 2.5×10^{13} to 6.0×10^{16} W/cm^2, as shown for each pulse duration in Table 1.

Table 1: Pulse durations d, energies E, and calculated peak irradiance I.

d (fs)	E (μJ)	I (W cm^{-2})
30	$10 - 2400$	$2.5 \times 10^{14} - 6.0 \times 10^{16}$
200	$25 - 2400$	$9.4 \times 10^{13} - 9.0 \times 10^{15}$
750	$25 - 2400$	$2.5 \times 10^{13} - 2.4 \times 10^{15}$
1500	$50 - 2400$	$2.5 \times 10^{13} - 1.2 \times 10^{15}$

To assess the presence of OB and SCE in water using this focusing geometry, the experimental setup shown in Figure 1(a) was employed. Emission spectra from the laser in water were collected at labeled positions (i) and (ii) with a compact fiber-coupled spectrometer (Ocean Optics, HR4000). Because OB forms an opaque plasma that results in scattering of the incident laser radiation, the detection of any scattered light perpendicular to the direction of beam propagation (position (i) in Figure 1(a)) indicates the presence of OB.[13] Significant spectral emission at position (i) was recorded even at the lowest pulse energies for each pulse duration (Figure 1(b)), which confirms operation above the critical electron density for OB,[13,14] which has recently been associated with the formation of cavitation bubbles at an electron density exceeding 1.8×10^{20} cm^{-3}.[7] These cavitation bubbles are visible in the photographs taken with 2400 μJ pulses of durations between 30 and 1500 fs (Figure 1(c)). The spectra of the laser beam following interaction with the water (position (ii) in Figure 1(a)) show that significant SCE is produced for 30 fs and 200 fs pulses, while no SCE is formed for 750 fs and 1500 fs pulses, even at the highest pulse energy (spectral plots in Figure 1(c)). The SCE obtained with 30 fs pulses exhibits emission at wavelengths lower

than 400 nm, which is similar to SCE spectra in water observed previously.[15,37] Finally, we note that the tight-focusing geometry results in no SCE on the quartz cuvette surface at any pulse duration (photographs in Figure 1(c)). The bright spot near the left side of the cuvette in the photograph of the 30 fs pulse does not result from white light in the quartz, it is an additional bright spot in the solvent itself, likely resulting from self-focusing of the beam in the quartz (Supporting Information, Figure S3).
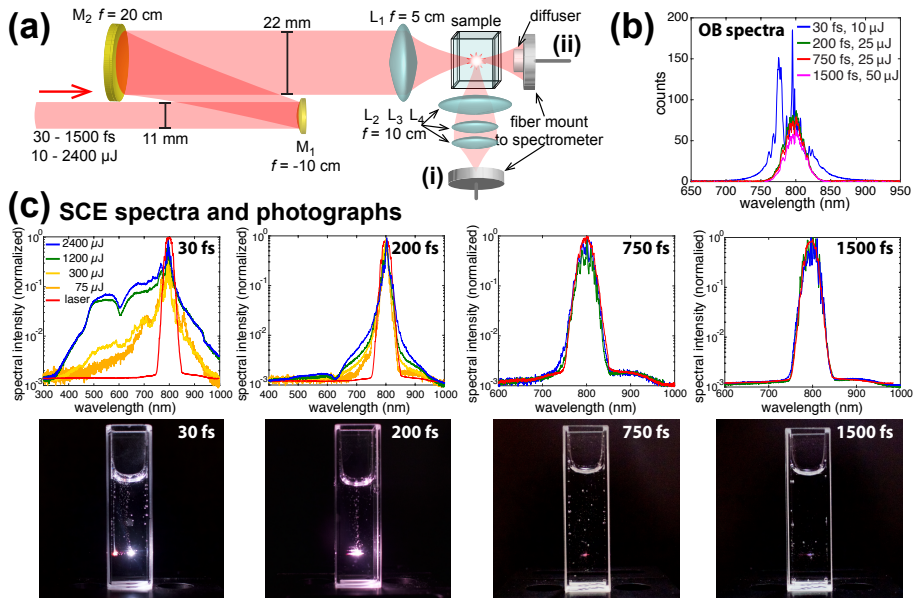

Figure 1: (a) Experimental setup showing locations of spectral measurements for OB (position (i)) and SCE (position(ii)). (b) Spectra of OB measured at lowest pulse energies for each pulse duration. (c) SCE spectra for each pulse duration at selected pulse energies.

For the photochemical reduction experiments, the laser beam was passed through a $10 \times 10 \times 40$ mm quartz fluorescence cuvette containing the prepared $KAuCl_4$ working solution (c.f., Section 2.1). The working solutions were irradiated for times ranging from 180 to 3600 seconds depending on the pulse energy and duration, sufficient to convert all of the $[AuCl_4]^-$ to AuNPs. In order to monitor the kinetics of $[AuCl_4]^-$ reduction during irradiation, the irradiation experiments were carried out in a home-built in situ UV-vis spectrometer consisting of a stabilized Deuterium-Tungsten light source (Ocean Optics, DH2000-BAL), optical fibers, two pairs of off-axis parabolic mirrors, and a compact spectrometer (Ocean Optics, HR4000) similar to the instrument in ref.[25]

6

2.3   Quantification of H_2O_2

Titanium dioxide (Sigma Aldrich); potassium permanganate (Alfa Aesar); sulfuric acid, hydrogen peroxide, and sodium oxalate (Fisher Scientific), were used as received. Hydrogen peroxide produced from laser irradiation of water was quantified using two different methods for comparison.

The first method of H_2O_2 quantification was adapted from ref,[39] where titanium(IV) sulfate (25 mM) was prepared by digesting a weighed amount of TiO_2 in concentrated H_2SO_4 for approximately 16 hours. The titanium(IV) sulfate (Ti^{4+}) reacts with H_2O_2 to form pertitanic acid (eq 1), resulting in a yellow solution. The intensity of the yellow color is directly related to the amount of H_2O_2 present, and may be quantified by measuring the absorbance at 407 nm.

$$Ti^{4+} + H_2O_2 + 2\,H_2O \longrightarrow TiO_2H_2O_2 + 4\,H^+ \tag{1}$$
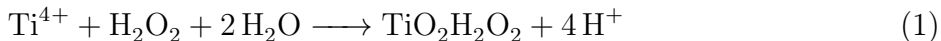
A calibration curve was constructed by measuring the absorbance at 407 nm of several solutions containing a range of $[H_2O_2]$. The UV-vis spectra of the different solutions can be found in the Supporting Information, Figure S4. All solutions contained 3.3 mM titanium(IV) sulfate. The H_2O_2 solution used to construct the calibration curve was standardized by titration, using a standardized solution of $KMnO_4$.[40] The $KMnO_4$ itself was standardized by titrating weighed amounts of sodium oxalate, following the procedure in ref.[41]

Once the titanium(IV) sulfate was calibrated against the standardized H_2O_2 solution, it was used to quantify the amount of H_2O_2 produced from irradiating 3 mL distilled water for 180 seconds over a range of laser pulse energies (2400, 1200, 600, 300, and 150 μJ), and pulse durations (30, 200, 750, and 1500 fs) (c.f., Section 2.2). Once the water was irradiated, 0.4 mL titanium(IV) sulfate (25 mM) was added to the cuvette, mixed, and the absorbance at 407 nm was measured. The means and standard deviations are reported and discussed in

Section [4.2](). Each laser condition set was measured in triplicate.

The second method used to quantify the production of H_2O_2 as a function of laser irradiation was by titration with $KMnO_4$.[40] The same condition sets as used in the titanium(IV) sulfate quantification method were were also used in triplicate on distilled water (3 mL). Immediately after termination of laser irradiation, H_2SO_4 (0.1 mL, 2 M) was added to the solution, and $KMnO_4$ was stirred in dropwise until the solution maintained a light-pink color, signifying the endpoint. The $KMnO_4$ was prepared by dissolving $KMnO_4$ into deionized water, and was standardized by titrating with sodium oxalate, according to the procedure in ref.[41]

Hydrogen peroxide production as a function of laser energy and pulse duration is discussed in Section [4.2](), where the H_2O_2 quantities are reported using the titanium(IV) sulfate method. A correlation plot of H_2O_2 production with data from both the titanium(IV) sulfate and $KMnO_4$ method is provided in the Supporting Information, Figure S5. The slope of a linear fit of the correlation data confirms the two methods agree, with a value of 0.96.

2.4 Characterization

Transmission Electron Microscopy (TEM). AuNPs were visualized using TEM (JEOL JEM-1230 TEM). The colloidal AuNPs were drop-casted onto a carbon-coated grid (Ted Pella, Inc.) and left to dry for 24 hours or longer. Average sizes and size distributions of the samples were measured using ImageJ software, which referenced a minimum of 500 particles from images of three separate areas of the TEM grid.

UV-vis spectroscopy. Ultraviolet-visible spectra were acquired with a Deuterium-Tungsten light source (Ocean Optics, DH2000-BAL), optical fibers, two pairs of off-axis parabolic mirrors, and a compact spectrometer (Ocean Optics, HR4000) similar to the instrument in ref.[25] Quartz cuvettes (1cm path cell, 3.5 mL capacity) were used, as the spectra encompassed a range from 220 to 1100 nm.

2.5 Theory

The interactions of ultrashort laser pulses and a dielectric medium with a band-gap exceeding the photon energy can produce quasi-free electrons in the conduction band through nonlinear multiphoton and tunneling photoionization;[42] and through collisions between high-kinetic-energy free electrons and neutral molecules resulting in avalanche, or cascade, ionization.[9] These processes result in the optical breakdown of the medium, forming an opaque plasma and cavitation bubbles, when the free-electron density ρ_e exceeds a critical value of $\rho_e \sim 10^{18} - 10^{21}$ cm^{-3}.[7–12]

We consider a laser pulse propagating in the z direction with time-dependent Gaussian intensity envelope[43,44]

$$I(z,t) = \frac{P(t,z)}{A(z)} = \frac{E_p}{\tau_p \pi w(z)^2} \exp\left[(-4\ln 2)\left(\frac{t - z/c}{\tau_p}\right)^2\right] \tag{2}$$

where E_p is the pulse energy, τ_p is the pulse duration, and c is the speed of light. The beam waist $w(z)$ at position z is based on the propagation of a Gaussian beam

$$w(z) = w_0\sqrt{1 + \frac{z^2}{z_R^2}} \tag{3}$$

where w_0 is the beam waist at the focus and z_R is the Rayleigh range. These quantities were measured to be $w_0 = 6.52 \times 10^{-4}$ cm and $z_R = 7.77 \times 10^{-3}$ cm, respectively, under our focusing conditions (c.f., Section 2.2 and Supporting Information, Figure S2). The aqueous medium is modeled as a dielectric with a band-gap $\Delta = 6.5$ eV.[8,10–12,44,45] The effective ionization potential $\tilde{\Delta}$ must account for the oscillation energy of the electron caused by the intense laser electric field,[42]

$$\tilde{\Delta} = \Delta + \frac{e^2 E^2}{4m\omega^2}, \tag{4}$$

where e is the electron charge, E is the electric field strength, ω is the center laser frequency, and m is the reduced mass of the exciton $1/m = 1/m_e + 1/m_h \simeq 0.5m_e$ based on the electron

and hole masses m_e and m_h, respectively.

The time evolution of the free-electron density ρ_e produced by the laser–water interaction is governed by the differential equation[11,12]

$$\frac{\partial \rho_e}{\partial t} = W_{\text{photo}} + W_{\text{casc}}\rho_e - W_{\text{diff}}\rho_e - W_{\text{rec}}\rho_e^2. \tag{5}$$

The production of free electrons is governed by the photoionization rate W_{photo} and cascade ionization rate W_{casc}, while electrons are lost from the focal volume through the diffusion rate W_{diff}, and recombination rate W_{rec}. The formulas for each rate are discussed below.

Photoionization may proceed via multiphoton absorption, electron tunneling, or both, depending on the peak irradiance and wavelength of the laser pulse. The transition from multiphoton to tunnel ionization is determined by the Keldysh adiabaticity parameter γ given by the ratio of the laser frequency ω to the electron tunneling frequency ω_t[42]

$$\gamma = \frac{\omega}{\omega_t} = \omega \frac{\sqrt{2m_e\Delta}}{eE}, \tag{6}$$

where multiphoton ionization dominates when $\gamma \gg 1$ and tunnel ionization dominates when $\gamma \ll 1$. The associated multiphoton ionization rate is given by[42]

$$W_{\text{MPI}} = \frac{2\omega}{9\pi}\left(\frac{m\omega}{\hbar}\right)^{3/2}\left(\frac{1}{16\gamma^2}\right)^n \Phi\left(\sqrt{2n - 2\frac{\tilde{\Delta}}{\hbar\omega}}\right)\exp\left[2n\left(1 - \frac{1}{4\gamma^2}\right)\right] \tag{7}$$

where n is the multiphoton order $n = [\frac{\tilde{\Delta}}{\hbar\omega} + 1]$ and $[\cdot]$ denotes the integer part, $\tilde{\Delta}$ is given by eq 4 and γ by eq 6. The function Φ is the Dawson integral, which is calculated numerically using an open source MATLAB code.[46] At sufficiently high intensities where $\gamma \ll 1$, the tunnel ionization rate applies[42]

$$W_{\text{tun}} = \frac{2\Delta}{9\pi^2\hbar}\left(\frac{m\Delta}{\hbar^2}\right)^{3/2}\left(\frac{\hbar\omega}{\Delta\gamma}\right)^{5/2}\exp\left[-\frac{\pi\gamma\Delta}{2\hbar\omega}\left(1 - \frac{\gamma^2}{8}\right)\right]. \tag{8}$$

In the intermediate range of $1 \leq \gamma \leq 1.3$, a weighted average of the ionization rates in eqs 7 and 8 are used,[45] which ensures a correct photoionization rate at all values of γ (Supporting Information, Figure S6).

The cascade ionization rate depends on the density of free electrons that have sufficiently high kinetic energy to undergo inverse Bremsstrahlung absorption of photons, leading to further generation of free electrons through collisions. On the basis of previous work, the time between electron–water collisions has been estimated at $\tau_c \sim 1.6 - 1.7$ fs;[8,47] we use the value $\tau_c = 1.7$ fs. The critical kinetic energy of the electrons for inverse Bremsstrahlung to occur is taken as $3/2\tilde{\Delta}$.[8] With these assumptions, the cascade-ionization rate becomes[8,44]

$$W_{\text{casc}} = \frac{1}{\omega^2 \tau_c^2 + 1} \left[\frac{e^2 \tau_c}{c n_0 \varepsilon_0 m (3/2)\tilde{\Delta}} I(t - \tau_{\text{ret}}, z) - \frac{m\omega^2 \tau_c}{M} \right], \tag{9}$$

where $\tau_{\text{ret}} = n\tau_c$ with n being the multiphoton order, $n_0 = 1.33$ is the refractive index of water, ε_0 is the vacuum permittivity, and M is the mass of the water molecule.

Free electrons formed by photoionization and cascade ionization may be lost from the focal volume via diffusion and recombination. Assuming an ellipsoidal focal volume defined by the beam waist w_0 and Rayleigh range z_r, the diffusion rate W_{diff} is given by[8,11]

$$W_{\text{diff}} = \frac{5\tau_c \tilde{\Delta}}{6m} \left[\frac{6}{w_0^2} + \frac{2}{z_r^2} \right]. \tag{10}$$

The recombination rate W_{rec} is taken as the widely-used empirical value[48]

$$W_{\text{rec}} = 2 \times 10^{-9} \ \text{cm}^3/\text{s} \tag{11}$$

While eq 11 oversimplifies the decay of free electrons by neglecting electron hydration and subsequent decay,[49,50] any recombination losses are slow compared to the pulse durations used in this work and thus play only a small role.

Equation 5 coupled to eqs 7-11 was solved using the Runge-Kutta integrator `ode45`

incorporated into MATLAB. Solving eq 5 for the experimentally used pulse durations of 30, 200, 750 and 1500 fs (all durations fwhm), the critical irradiance to cause optical breakdown at each pulse duration was determined using the threshold of $\rho_e = 1.8 \times 10^{20}$ cm^{-3} based on the cavitation bubble threshold recorded in a recent study.[7] Figure 2 shows the time-evolution of the free-electron density ρ_e at 30 fs (blue), 200 fs (green), 750 fs (red), and 1500 fs (magenta); the associated peak-irradiances in W cm^{-2} are indicated in the legend. The value of zero on the time-axis corresponds to the center of the pulse. The decreasing irradiance needed to reach the optical breakdown threshold as the pulse duration lengthens from 30 to 1500 fs is due to the increasing participation of cascade ionization (eq 9) in the production of free electrons at longer pulse durations, as noted in earlier work.[8,12]
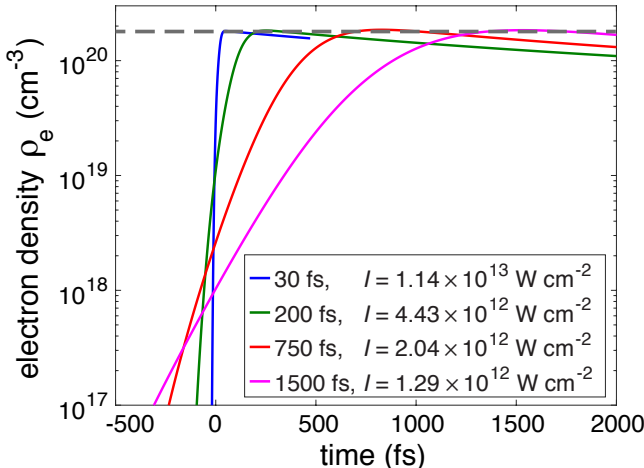

Figure 2: Time evolution of the free-electron density ρ_e as a function of time immediately following interaction with pulses with durations of 30 fs (blue), 200 fs (green), 750 fs (red), and 1500 fs (magenta), at the irradiances indicated in the legend. The maximum value of ρ_e is 1.8×10^{20} cm^{-3}, as indicated by the gray-dashed line.

Because the peak-irradiance range of 2.5×10^{13} to 6.0×10^{16} W cm^{-2} significantly exceeds the threshold-irradiance for optical breakdown at all pulse durations, we wish to estimate the plasma volume in which the electron density exceeds the OB threshold under our experimental conditions. Of particular interest is the growth of the plasma volume with peak-irradiance due to the widely recognized role of electrons generated from OB and SCE in the photo-chemical reduction of $[\text{AuCl}_4]^-$ and other metal salts.[16–18,21,22,25,27] To estimate the plasma

volume, we first calculate the critical propagation distance z_{crit} in front of the focus where OB begins, based on Gaussian beam propagation via eq 3. While the approximation of Gaussian beam propagation at high irradiance near the geometric focus neglects nonlinear beam propagation phenomena and thus will result in a crude approximation of z_{crit} and the true plasma volume,[8,13,14,38] our goal is to estimate the growth of the plasma volume with pulse energy over a wide range of pulse durations and not to model the propagation of any particular pulse in the medium nor calculate the exact plasma volume. Thus, we must assume that the error in the value of z_{crit} does not change dramatically over the experimental pulse energy range. This assumption is reasonable because the peak-irradiance range exceeds the optical breakdown threshold by a factor of 10 at even the lowest pulse energy used for each pulse duration in the experiments (Figure 2 and Table 1).
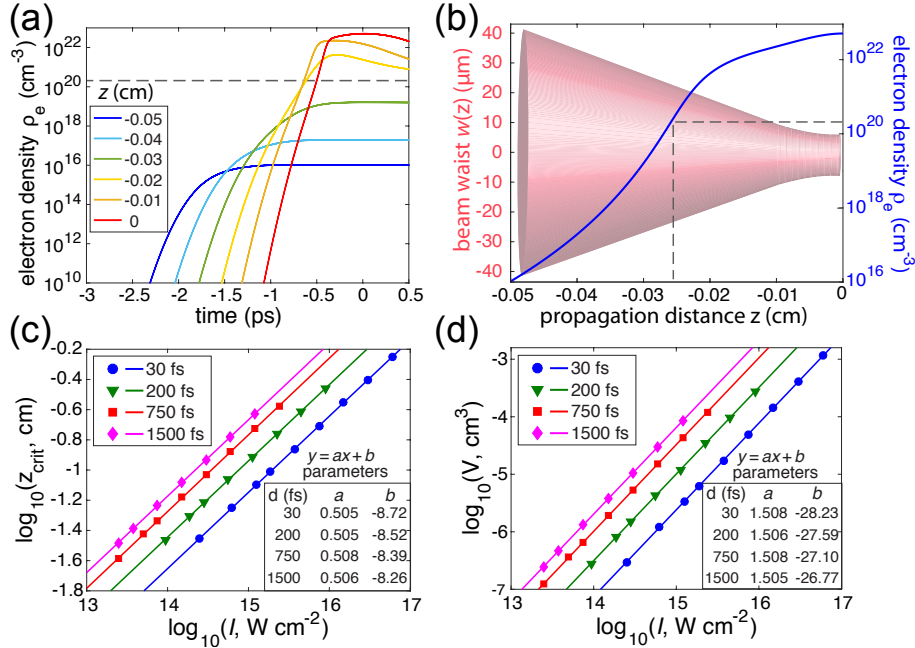

Figure 3: (a) Calculated electron density ρ_e as a function of time for a 750 fs, 25 μJ pulse at a series of propagation distances between $z = -0.05$ cm and the focus at $z = 0$ cm. (b) Peak ρ_e as a function of z (blue curve) overlaid with the spatial profile of the Gaussian beam. In both panels, the dashed gray lines denote the plasma threshold $\rho_e = 1.8 \times 10^{20}$ cm^{-3}. Calculated values of z_{crit} (c) and plasma volume V (d) as a function of irradiance I for 30 fs (blue circles), 200 fs (green triangles), 750 fs (red squares), and 1500 fs (magenta diamonds) pulses, with linear fits (solid lines) and fitting coefficients given in the legends.

To identify z_{crit}, eq 5 was propagated for each pulse energy and duration used in our experiments at a series of propagation distances $z < 0$ cm (i.e., just before the focal spot at $z = 0$ cm) in order to determine the highest electron density achieved as a function of propagation distance z. The results for time-dependent electron density produced by 750 fs, 25 μJ pulses at a series of z values is shown in Figure 3(a). The maximum electron density as a function of z is shown in Figure 3(b) (blue line, right ordinate axis), superimposed on the spatial profile of the Gaussian beam (red volume, left ordinate axis). In both panels, the electron density threshold of $\rho_e = 1.8 \times 10^{20}$ cm^{-3} is indicated by a gray-dashed line. The peak electron density achieved as a function of z was calculated using these methods for each pulse energy and duration used in the experiments (Supporting Information, Figure S7) and the associated values of z_{crit} determined at each pulse duration and energy. At all pulse durations, the absolute value of z_{crit} was found to grow with irradiance I as approximately $I^{1/2}$, as shown in Figure 3(c).

While rigorous calculations of the spatial distribution of electron density obtained from propagating femtosecond pulses in water reveal a variety of plasma volume shapes depending on the focusing-geometry and pulse duration,[13,38] the plasma volume can be approximated by simple geometric shapes such as an ellipsoid with dimensions based on the numerical aperture.[8,51] Here, we estimate the plasma volume using the obtained values of z_{crit}; approximating the plasma volume with any three-dimensional shape such as an ellipsoid, cylinder, or cone will result in the plasma volume growing as z_{crit}^3. Thus, while the particular choice of shape will determine the calculated *value* of the plasma volume at any given pulse duration and irradiance, the choice of shape will not affect the *growth* of the plasma volume with peak irradiance I, which will grow as $V \propto I^{3/2}$ based on the relation $z_{\text{crit}} \propto I^{1/2}$. For simplicity, we approximate the volume by a cone with height $|z_{\text{crit}}|$ and radius $w(z_{\text{crit}})$ based on the measured beam diameters fit with eq 3. The resulting plasma volumes and fit values are shown in Figure 3(d), confirming that the volume grows as $I^{3/2}$. We will connect these results on the growth of the plasma volume with peak irradiance at each pulse duration with

14

the observed $[AuCl_4]^-$ reduction kinetics in Section 4.

3 Results

3.1 Photochemical reduction of $[AuCl_4]^-$

The photochemical conversion of $[AuCl_4]^-$ to AuNPs may be easily monitored by UV-vis spectroscopy through tracking the time-dependent consumption of the ligand-metal charge transfer (LMCT) peak of $[AuCl_4]^-$ and growth of the surface plasmon resonance (SPR) peak of AuNPs. Representative UV-vis spectra showing conversion of $[AuCl_4]^-$ to AuNPs in the focused geometry using 2400 μJ pulses with durations 30 fs, 200 fs (negative chirp), 200 fs (positive chirp), 750 fs, and 1500 fs are shown in Figures 4(a) through (e). From these spectra, the irradiation time required for complete conversion of $[AuCl_4]^-$ to AuNPs is determined as the time where the absorbance of the SPR peak ceases growth, as shown by the plot of SPR absorbance versus irradiation time in Figure 4(f), where the completion time τ for each pulse duration is marked with an 'x'. Using this determined value of τ and the associated UV-vis spectrum containing only AuNPs, the concentration of $[AuCl_4]^-$ at intermediate times when both $[AuCl_4]^-$ and AuNPs are present in the solution may be obtained by isolating the $[AuCl_4]^-$ contribution to absorbance in the UV region of the spectra.[25] Specifically, when both $[AuCl_4]^-$ and AuNPs are present in solution, the recorded absorbance at $\lambda = 250$ nm will be the sum of the absorbances of both species. By quantifying the fractional content of AuNPs through monitoring the absorbance at $\lambda = 450$ nm (where $[AuCl_4]^-$ doesn't absorb) and subtracting off the expected corresponding AuNP absorbance at $\lambda = 250$ nm, the contribution of $[AuCl_4]^-$ to the absorbance at $\lambda = 250$ nm may be isolated. Further details are provided in the discussion in the Supporting Information and Figure S8. The resulting time-dependent concentration of $[AuCl_4]^-$ will be used to assess the reaction kinetics for all experiments in this work.
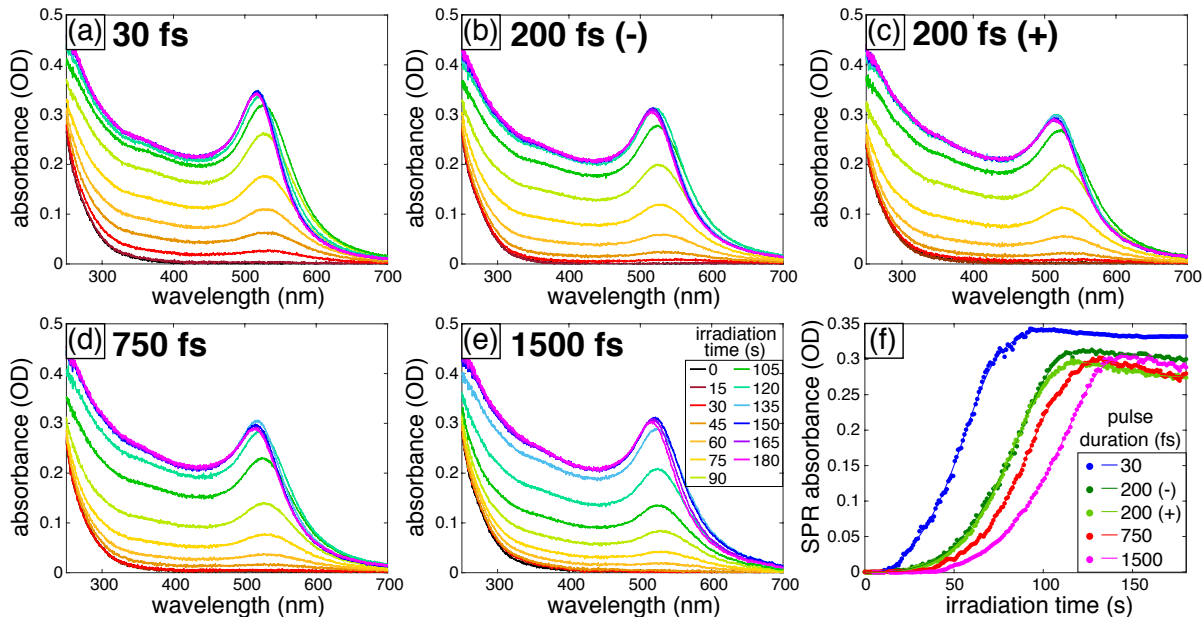
Figure 4: UV-vis spectra recorded during irradiation of aqueous $[AuCl_4]^-$ with 2400 μJ pulses with durations 30 fs (a); 200 fs, negative chirp (b); 200 fs, positive chirp (c); 750 fs (d), and 1500 fs (e). The spectra recorded at different irradiation times are indicated by the colors associated with the legend in panel (e). Panel (f) shows the time-dependent absorbance of the SPR feature in the spectra (a) through (e), showing the required irradiation time for complete conversion of $[AuCl_4]^-$ to AuNPs.

While LaMer's classical nucleation and growth model[52] has been widely used to model the formation of metal nanoparticles,[53–55] numerous studies of metal nanoparticle growth kinetics have supported autocatalytic[32–34,56] and/or aggregative growth[57,58] mechanisms. In particular, previous studies of femtosecond laser-induced photochemical reduction of $[AuCl_4]^-$[25,27] have supported the applicability of the Finke-Watzky autocatalytic nucleation-growth rate law,[56]

$$-\frac{d[A]}{dt} = \frac{d[B]}{dt} = k_1[A] + k_2[A][B] \tag{12}$$

where [A] is the concentration of the precursor $[AuCl_4]^-$ and [B] is the concentration of the AuNPs. The rate constants k_1 and k_2 correspond to the rates of nucleation of metal clusters and autocatalytic growth into nanoparticles, respectively. Integration of eq 12 gives the

16

time-dependent precursor concentration[56]

$$[A(t)] = \frac{\frac{k_1}{k_2} + [A(0)]}{1 + \frac{k_1}{k_2[A(0)]}e^{(k_1+k_2[A(0)])t}} \tag{13}$$

where $[A(0)]$ is the initial precursor concentration. As we will discuss in detail below in Section 4, the nucleation rate constant k_1 depends on the volume of the OB plasma, i.e., the number of electrons available to reduce Au^{3+}, while the autocatalytic growth rate constant k_2 depends on the concentration of H_2O_2, which is needed to drive the surface mediated $[AuCl_4]^-$ reduction on AuNPs.[59–61]

To assess the dependence of the rate constants k_1 and k_2 on the pulse energy and duration, experiments were performed with pulses of the following durations and energies: 30 fs (negative chirp, $10 - 2400\,\mu J$), 200 fs (positive and negative chirp, $25 - 2400\,\mu J$), 750 fs (negative chirp, $25 - 2400\,\mu J$), and 1500 fs (negative chirp, $50 - 2400\,\mu J$). Figure 5 shows the concentration of $[AuCl_4]^-$ as a function of irradiation time for representative experiments conducted with (a) 2400 μJ pulses, (b) 75 μJ pulses, and (c) 6×10^{14} W cm^{-2} pulses. The experimental data are shown as circles and fit to eq 13 as solid lines. Representative plots for each pulse duration and energy are shown in the Supporting Information, Figure S9. The extracted rate constants fit to eq 13 at each pulse energy and duration are in Tables 2 (k_1) and 3 (k_2). Reported errors denote the standard deviation of the rate constants across more than five different experiments, which were conducted on at least three separate days. We note that the kinetics results for 200 fs pulses with positive and negative chirp (light and dark green curves in Figures 4(f) and 5) are the same, indicating that the direction of chirp has no effect on the kinetics. Thus, the remainder of this work will consider only the results for negatively chirped pulses. The significance of the relations between the k_1 and k_2 values and the peak irradiance will be discussed below in Section 4.
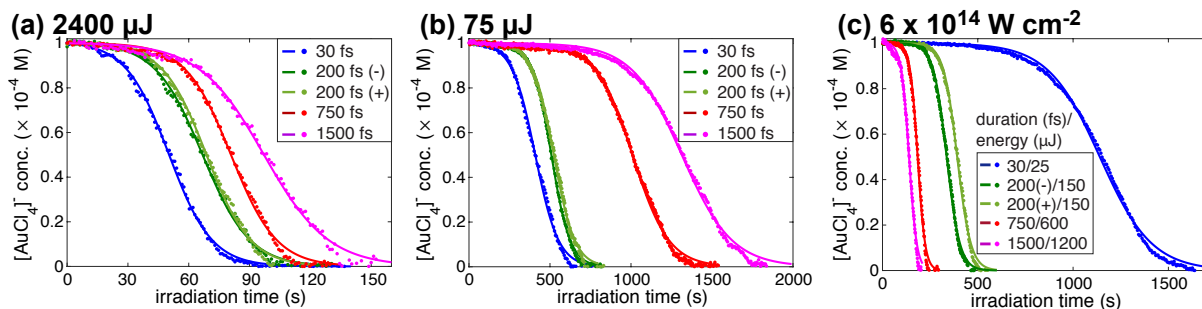
17

Figure 5: Representative plots of $[AuCl_4]^-$ versus irradiation time (circles), with fits to eq 13 (solid lines) for pulses with duration 30 fs (blue), 200 fs (negative/positive chirp, dark/light green), 750 fs (red), and 1500 fs (magenta). (a) 2400 μJ pulses. (b) 75 μJ pulses. (c) 6×10^{14} W cm^{-2} pulses, with pulse energies given in the legend.

Table 2: Values of rate constant k_1 from eq 13. Units are s^{-1}.

E (μJ)	30 fs	200 fs ($-$)	200 fs ($+$)	750 fs	1500 fs
2400	$8 \pm 3 \times 10^{-4}$	$1.9 \pm 0.8 \times 10^{-4}$	$2 \pm 1 \times 10^{-4}$	$8 \pm 5 \times 10^{-5}$	$1.4 \pm 0.2 \times 10^{-4}$
1200	$4 \pm 2 \times 10^{-4}$	$9 \pm 5 \times 10^{-5}$	$9 \pm 5 \times 10^{-5}$	$5 \pm 2 \times 10^{-5}$	$7 \pm 2 \times 10^{-5}$
600	$3 \pm 1 \times 10^{-4}$	$5 \pm 2 \times 10^{-5}$	$6 \pm 4 \times 10^{-5}$	$3 \pm 1 \times 10^{-5}$	$3 \pm 1 \times 10^{-5}$
300	$1.4 \pm 0.5 \times 10^{-4}$	$3 \pm 1 \times 10^{-5}$	$3 \pm 2 \times 10^{-5}$	$1.1 \pm 0.6 \times 10^{-5}$	$1.0 \pm 0.6 \times 10^{-5}$
150	$7 \pm 3 \times 10^{-5}$	$9 \pm 5 \times 10^{-6}$	$1.0 \pm 0.9 \times 10^{-5}$	$5 \pm 4 \times 10^{-6}$	$3 \pm 2 \times 10^{-6}$
75	$1.6 \pm 0.8 \times 10^{-5}$	$3 \pm 2 \times 10^{-6}$	$3 \pm 2 \times 10^{-6}$	$1.4 \pm 0.9 \times 10^{-6}$	$1.1 \pm 0.9 \times 10^{-6}$
50	$8 \pm 6 \times 10^{-6}$	$1.9 \pm 0.8 \times 10^{-6}$	$1.3 \pm 0.9 \times 10^{-6}$	$9 \pm 6 \times 10^{-7}$	$6 \pm 4 \times 10^{-7}$
25	$2 \pm 1 \times 10^{-6}$	$5 \pm 4 \times 10^{-7}$	$7 \pm 6 \times 10^{-7}$	$2 \pm 1 \times 10^{-7}$	
10	$5 \pm 4 \times 10^{-7}$				

Table 3: Values of rate constant k_2 from eq 13. Units are mM^{-1} s^{-1}.

E (μJ)	30 fs	200 fs ($-$)	200 fs ($+$)	750 fs	1500fs
2400	1.00 ± 0.08	0.89 ± 0.06	0.92 ± 0.04	0.92 ± 0.07	0.73 ± 0.07
1200	0.64 ± 0.09	0.65 ± 0.05	0.59 ± 0.04	0.64 ± 0.06	0.50 ± 0.02
600	0.41 ± 0.05	0.45 ± 0.03	0.46 ± 0.06	0.42 ± 0.03	0.32 ± 0.03
300	0.31 ± 0.03	0.36 ± 0.04	0.32 ± 0.6	0.27 ± 0.03	0.18 ± 0.02
150	0.22 ± 0.02	0.24 ± 0.02	0.21 ± 0.03	0.18 ± 0.02	0.126 ± 0.008
75	0.14 ± 0.02	0.15 ± 0.03	0.13 ± 0.02	0.10 ± 0.01	0.072 ± 0.006
50	0.113 ± 0.008	0.12 ± 0.02	0.10 ± 0.02	0.077 ± 0.008	0.037 ± 0.002
25	0.074 ± 0.009	0.067 ± 0.005	0.057 ± 0.009	0.053 ± 0.004	
10	0.043 ± 0.006				

3.2   Characterization of AuNP products

The particles were characterized for their size and size distribution by comparing the SPR peak of the finished AuNPs to corresponding TEM images. Figure 6 shows the final UV-vis spectra of AuNPs produced with 30 fs; 200 fs, negative chirp; 750 fs; and 1500 fs pulse durations (panels (a)-(d)) over a range of pulse energies (25-2400 μJ, labeled in panel (a)). For all pulse durations, an intensity increase of the SPR peak is observed as the laser energy is decreased, corresponding to a diameter increase in the spherical AuNPs.[62] There is also SPR peak-broadening and a red-shift in SPR wavelength in the AuNPs formed with lower laser energies, suggesting not only that the AuNP sizes are increasing, but that the particles are agglomerating.[23,62]
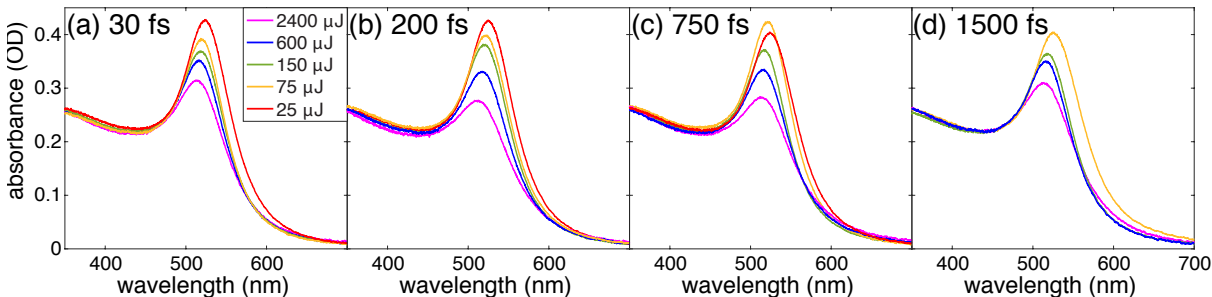

Figure 6:   UV-vis spectra recorded post-completion of aqueous $[AuCl_4]^-$ irradiation, with pulse durations of 30 fs (a); 200 fs, negative chirp (b); 750 fs (c); and 1500 fs (d). The spectra recorded at different laser energies are indicated by the colors associated with the legend in panel (a).

The trends of increasing AuNP size and aggomeration are also observed in the representative TEM images displayed in Figure 7. The histograms and average AuNP sizes displayed were calculated from approximately 500 AuNPs per sample, using ImageJ software. The average AuNP sizes vary within a $2.7 - 6.4$ nm diameter range, with some distributions having very broad standard deviations. Although there is no distinct trend between the average AuNP sizes at the two laser energies, visual observation of the TEM images shows that the AuNPs produced at 150 μJ contain larger AuNPs than their 2400 μJ counterparts for each pulse duration.
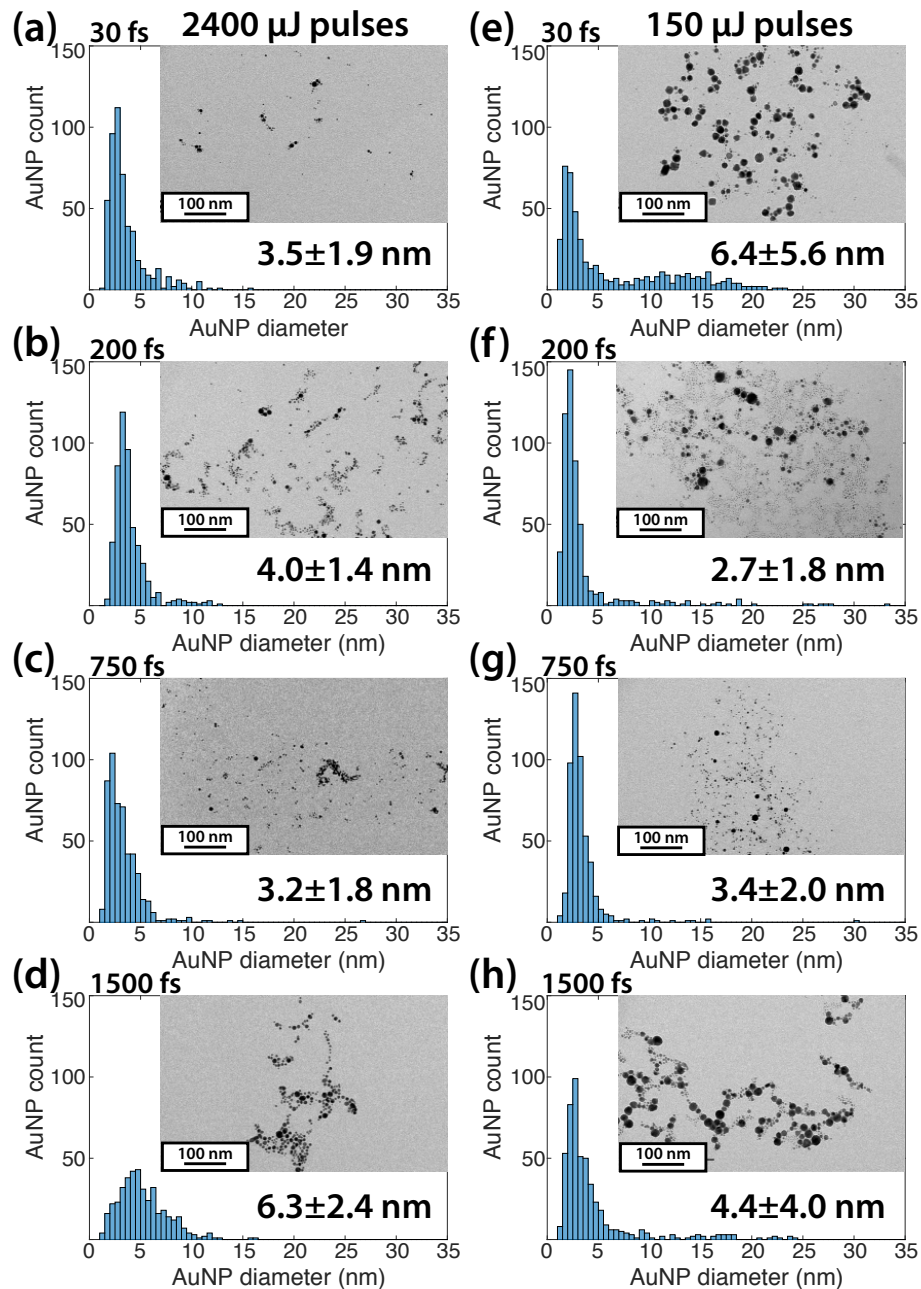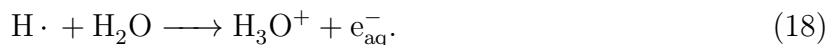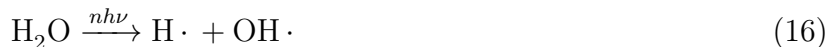
19

Figure 7: Representative TEM images and corresponding size distribution histograms of the AuNPs produced using 2400 μJ for 30 fs (a); 200 fs, negative chirp (b); 750 fs (c); 1500 fs (d) pulse durations; and 150 μJ for 30 fs (e); 200 fs, negative chirp (f); 750 fs (g); 1500 fs (h) pulse durations. All size distribution histograms are obtained from counting approximately 500 particles using ImageJ software. Mean particle sizes and standard deviations are reported.

The AuNPs formed with the 2400 μJ pulses had narrower size distributions and standard deviations (Figure 7, panels (a)-(d)) relative to the AuNPs formed with the 150 μJ pulses (Figure 7, panels (e)-(h)). While the particle size distributions in Figure 7(e)-(h) all exhibit tails that spread out toward larger diameters, the particle size increased most significantly for 30 fs pulses (Figure 7(e)). Histogram (e) shows a bimodal size distribution, with a sharp peak around $2-3$ nm and a broad peak around 12 nm, suggesting that small AuNPs (with $2-3$ nm diameters) start to agglomerate into masses around 12 nm in diameter. These observations are consistent with the broadening SPR peak in the UV-vis spectra in Figure 6, and the red-shifted tail forming for the spectra associated with AuNPs produced at low pulse energy with all pulse durations. This observed increase in AuNP size with lower pulse energy is consistent with previous results using 36 ps laser pulses, where the AuNP size increased from 5.8 ± 1.1 nm using 1800 μJ pulses to 9.6 ± 2.7 nm using 400 μJ pulses when a capping agent was added to control particle size.[23] At the high pulse energy of 2400 μJ, the AuNP sizes are noticeably larger for 1500 fs pulses (Figure 7(d)) as compared to $30-750$ fs pulses (Figure 7, panels (a)-(c)). This result suggests that at a high pulse energy, a long pulse duration may produce slightly larger AuNPs, which is consistent with previous results showing formation of 4.8 ± 1.9 nm AuNPs when irradiating a 0.1 mM $[\mathrm{AuCl_4}]^-$ solution of similar pH using 2500 μJ, 36 ps laser pulses.[25] Collectively, the present results suggest that both the pulse energy and duration may be used to control the size and dispersity of AuNPs in the absence of a capping agent. More in-depth characterization of the uncapped AuNPs synthesized here, including their catalytic activity and stability over time, will be further investigated and reported in a future work.

4   Discussion

The primary importance of water photolysis in OB microplasmas to the photochemical reduction of $[\mathrm{AuCl_4}]^-$ and other metal salts is well-established.[16–18,21,22,25,27] The photolysis

reactions involved include[21,49,50,63,64]

$$H_2O \xrightarrow{nh\nu} e^- + H^+ + OH\cdot \tag{14}$$

$$e^- \longrightarrow e^-_{aq} \tag{15}$$

$$H_2O \xrightarrow{nh\nu} H\cdot + OH\cdot \tag{16}$$

$$2\,OH\cdot \longrightarrow H_2O_2 \tag{17}$$

$$H\cdot + H_2O \longrightarrow H_3O^+ + e^-_{aq}. \tag{18}$$

While both hydrated electrons and hydrogen radicals are capable of reducing $[AuCl_4]^-$, the fast consumption of $H\cdot$ via eq 18 observed in water photolysis with picosecond pulses[49] suggests that the contribution of $H\cdot$ to the $[AuCl_4]^-$ reduction rate will be negligible. In contrast, hydrated electrons may be formed from both the free electrons generated in OB plasma via eq 15 within several hundred femtoseconds[50,64] and from the reaction of water with $H\cdot$ via eq 18. Hydrated electrons have lifetimes of up to hundreds of nanoseconds in pure water[65] and react with $[AuCl_4]^-$ with a diffusion-controlled rate constant of 6.1×10^{10} $M^{-1}\,s^{-1}$.[66] Thus, hydrated electrons are expected to be the dominant $[AuCl_4]^-$ reducing agent[21] through the reaction

$$[AuCl_4]^- + 3\,e^-_{aq} \longrightarrow Au(0) + 4\,Cl^-. \tag{19}$$

In addition to $[AuCl_4]^-$ reduction by hydrated electrons, the H_2O_2 generated in eq 17 can reduce $[AuCl_4]^-$ in the presence of AuNPs[22,25,59–61] via the autocatalytic reaction

$$[AuCl_4]^- + \frac{3}{2}H_2O_2 + Au_m \longrightarrow Au_{m+1} + \frac{3}{2}O_2 + 3\,HCl + Cl^-. \tag{20}$$
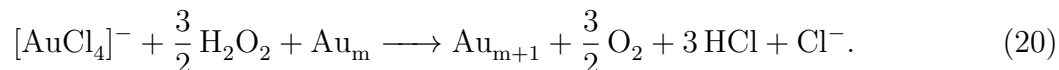
Below, we will demonstrate that the formation of electrons in the OB microplasma is directly proportional with the observed value of the first-order rate constant k_1 in eq 13, while the formation rate of H_2O_2 is correlated to the value of the k_2 rate constant.

4.1 Electron formation and rate constant k_1

The experimental k_1 values from Table 2 for pulses with durations of 30 fs (blue circles), 200 fs (green triangles), 750 fs (red squares), and 1500 fs (magenta diamonds) are plotted as functions of peak irradiance in Figure 8(a). For pulse energies of 600 μJ and below (1200 μJ for 1500 fs pulses), the k_1 values were fit to linear functions in log-log space (solid lines, Figure 8(a)) and the resulting slopes are listed in the legend. The slopes are all approximately 1.5, which is consistent with the slope of the calculated plasma volumes with peak intensity (Figure 3(d)). This result suggests that the k_1 values are related to the volume of the OB plasma where the electron density exceeds the critical threshold of 1.8×10^{20} cm^{-3} (c.f., the discussion in Section 2.5).
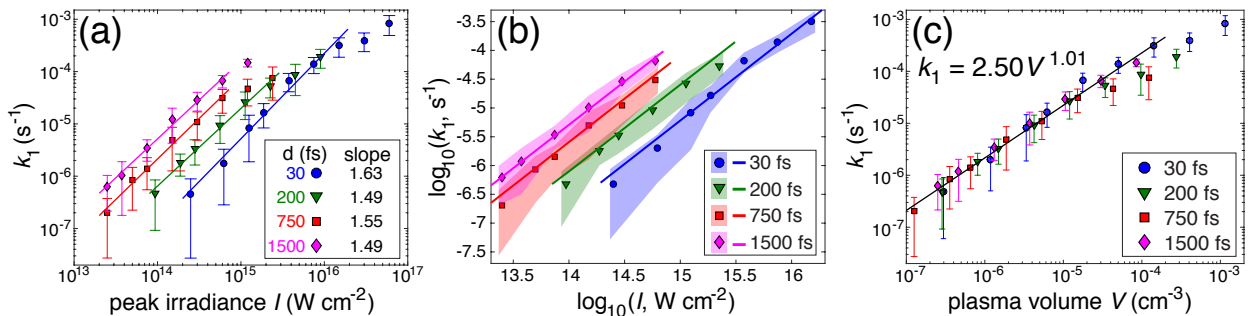

Figure 8: (a) Rate constant k_1 as a function of peak irradiance for each pulse duration. (b) Rate constant k_1 as a function of peak irradiance, overlaid with calculated plasma volumes (solid lines). (c) Rate constant k_1 versus calculated plasma volume, showing a direct correlation with the power law of 1.01.

To further explore the link between the plasma volume and k_1 value, the calculated plasma volumes were directly compared to the the k_1 values by plotting both quantities as functions of peak irradiance in log-log space (Figure 8(b)). The plasma volumes (solid lines) are shifted by 0.4 units on the ordinate axis to most closely match the experimental k_1 values (colored symbols) and error ranges (transparent shaded regions). Importantly, the *relative* spacing of the plasma volumes for each pulse duration from Figure 3(d) was not changed in Figure 8(b), which suggests that the same relation between plasma volume and k_1 value holds, regardless of pulse duration. To confirm this assertion, the experimental k_1 values

were plotted as a function of the calculated plasma volume at the same pulse duration and peak irradiance (Figure 8(c)), with the best fit equation for pulse energies below 600 μJ (black solid line) confirming the direct proportionality of the plasma volume and k_1 value. At high pulse energies, the k_1 values are lower than would be expected based on the plasma volume, suggesting saturation of electron formation, likely due to intensity clamping that occurs at high peak irradiance.[13–15]

4.2 H_2O_2 formation and rate constant k_2

While the contribution of H_2O_2 to the formation of gold nanoparticles by photochemical reduction of $[AuCl_4]^-$ has been well-documented,[22–26,60,61] a quantitative relationship between the rate of H_2O_2 formation and the autocatalytic reduction rate has yet to be established. For each pulse duration, and at pulse energies of 150 μJ and higher, the amount of H_2O_2 formed after laser irradiation of pure water for 180 seconds was quantified using the two methods described in Section 2.3. The measured H_2O_2 yields using the two methods were comparable (Supporting Information, Figure S4), and the titanium sulfate measurements are used here. The formation rate of H_2O_2 was extracted from these measurements based on the previously observed linear increase in H_2O_2 concentration with irradiation time upon femtosecond laser irradiation of pure water.[22]

The k_2 values for pulses with duration 30 fs (blue circles), 200 fs (green triangles), 750 fs (red squares), and 1500 fs (magenta diamonds) are plotted as functions of peak irradiance in Figure 9(a). For each pulse duration, the growth of k_2 with peak irradiance was fit to a linear function in log-log space (solid lines on Figure 9(a)); the resulting slopes are indicated in the legend. The k_2 values exhibit a weaker dependence on peak irradiance I than the k_1 values, with the values growing as $k_2 \sim I^{0.5} - I^{0.6}$, depending on pulse duration, as opposed to $k_1 \sim I^{1.5}$. The formation rate of H_2O_2 exhibits a stronger dependence on the peak irradiance at all pulse durations, with $[H_2O_2] \sim I$ (Figure 9(b)). As a result, the k_2 values grow with H_2O_2, but approximately as $k_2 \sim [H_2O_2]^{0.5}$ (Figure 9(c)).
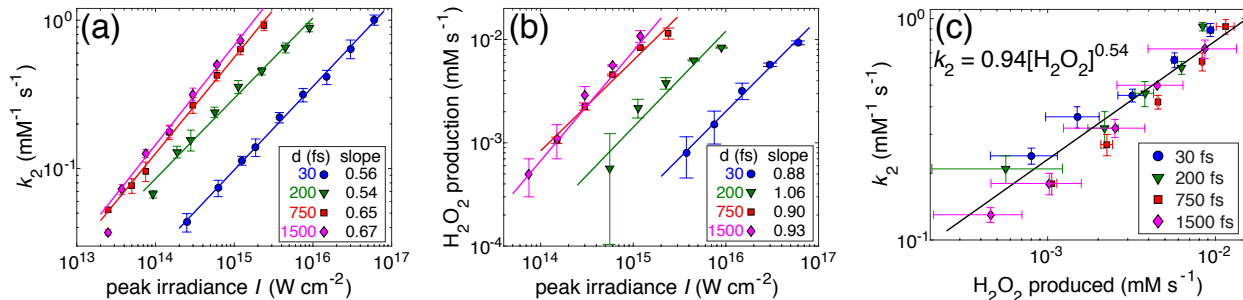
Figure 9: (a) Rate constant k_2 as a function of peak laser intensity for each pulse duration. (b) H_2O_2 formation rate as a function of peak irradiance. (c) Rate constant k_2 versus H_2O_2 formation rate.

5   Conclusion

This work has quantified the roles played by free electrons and H_2O_2 formation in driving the photochemical reduction of $[AuCl_4]^-$ into AuNPs using intense, ultrafast laser pulses. The autocatalytic $[AuCl_4]^-$ reduction kinetics were monitored using *in situ* UV-vis spectroscopy. The growth of the optical breakdown plasma volume with peak irradiance as $V \sim I^{1.5}$ matched the growth of the first-order rate constant, k_1, with peak irradiance, thereby indicating that free electron formation from optical breakdown of water is directly proportional to the rate of nucleation of Au atoms under our experimental conditions. By quantifying the formation rate of H_2O_2 as a function of pulse energy and duration, we found that the H_2O_2 formation rate was directly proportional to the irradiance at each pulse duration, i.e., $H_2O_2 \sim I$. The second-order rate constant, k_2, depended on peak irradiance through the relationship $k_2 \sim I^{0.5}$, and was found to follow the same relationship of $k_2 \sim H_2O_2{}^{0.5}$ at all pulse durations. These results have determined, for the first time, quantitative relationships between the $[AuCl_4]^-$ reduction rate and the two chemical species that have long been proposed as the dominant reducing agents operating in femtosecond laser-assisted reduction of $[AuCl_4]-$ to AuNPs.[16–18,21–27]

By characterizing the resulting sizes and size distributions of the AuNP products across irradiation conditions, we found a stronger relationship between the AuNP size and pulse energy than for pulse duration, where the primary small AuNPs ($\sim 2-3$ nm) were found to

agglomerate into larger $\sim 10 - 20$ nm particles. However, a doubling of the average AuNP size was observed when increasing the pulse duration from 750 fs to 1500 fs. The observed trends with both pulse energy and duration likely arise from the stronger dependence of the plasma volume (i.e., electron formation) on the peak irradiance as compared to the H_2O_2 formation. At low pulse energy, the concentration of H_2O_2 in the OB plasma will therefore be higher *relative* to the electron density, thereby favoring formation of fewer Au nuclei and increasing sizes of existing AuNPs through autocatalytic growth and agglomeration. Thus, understanding how the laser pulse parameters influence the chemical composition of the OB plasma may enable improved tuning of metal NP sizes and other properties. For instance, these findings may facilitate optimization of NP synthesis conditions in other metal systems where the production of H_2O_2 in the OB plasma may play a more detrimental role (e.g. oxidation of AgNPs to Ag^+ in the presence of H_2O_2).

Acknowledgement

Supporting Information Available

Characterization of pulse durations and focusing conditions, additional experimental and theoretical details, additional kinetics and TEM data.

This material is available free of charge via the Internet at http://pubs.acs.org/.

References

(1) Kandidov, V.; Kosareva, O.; Golubtsov, I.; Liu, W.; Becker, A.; Akozbek, N.; Bowden, C.; Chin, S. Self-Transformation of a Powerful Femtosecond Laser Pulse into a White-Light Laser Pulse in Bulk Optical Media (or Supercontinuum Generation). *Appl. Phys. B* **2003**, *77*, 149–165.

(2) Stelmaszczyk, K.; Rohwetter, P.; Méjean, G.; Yu, J.; Salmon, E.; Kasparian, J.; Ackermann, R.; Wolf, J.-P.; Wöste, L. Long-Distance Remote Laser-Induced Breakdown Spectroscopy Using Filamentation in Air. *Appl. Phys. Lett.* **2004**, *85*, 3977–3979.

(3) Odhner, J. H.; McCole, E. T.; Levis, R. J. Filament-Driven Impulsive Raman Spectroscopy. *J. Phys. Chem. A* **2011**, *115*, 13407–13412.

(4) Shen, M.; Carey, J. E.; Crouch, C. H.; Kandyla, M.; Stone, H. A.; Mazur, E. High-Density Regular Arrays of Nanometer-Scale Rods Formed on Silicon Surfaces via Femtosecond Laser Irradiation in Water. *Nano Lett.* **2008**, *8*, 2087–2091.

(5) Vitek, D. N.; Block, E.; Bellouard, Y.; Adams, D. E.; Backus, S.; Kleinfeld, D.; Durfee, C. G.; Squier, J. A. Spatio-Temporally Focused Femtosecond Laser Pulses for Nonreciprocal Writing in Optically Transparent Materials. *Opt. Express* **2010**, *18*, 24673–24678.

(6) Antkowiak, M.; Torres-Mapa, M. L.; Stevenson, D. J.; Dholakia, K.; Gunn-Moore, F. J. Femtosecond Optical Transfection of Individual Mammalian Cells. *Nat. Protocols* **2013**, *8*, 1216–1233.

(7) Linz, N.; Freidank, S.; Liang, X.-X.; Vogel, A. Wavelength Dependence of Femtosecond Laser-Induced Breakdown in Water and Implications for Laser Surgery. *Phys. Rev. B* **2016**, *94*, 024113.

(8) Vogel, A.; Noack, J.; Hüttman, G.; Paltauf, G. Mechanisms of Femtosecond Laser Nanosurgery of Cells and Tissues. *Appl. Phys. B* **2005**, *81*, 1015–1047.

(9) Shen, Y. R. *The Principles of Nonlinear Optics*; Wiley: New York, 1984.

(10) Sacchi, C. A. Laser-Induced Electric Breakdown in Water. *J. Opt. Soc. Am. B* **1991**, *8*, 337–345.

(11) Kennedy, P. K. A First-Order Model for Computation of Laser-Induced Breakdown Thresholds in Ocular and Aqueous Media. I. Theory. *IEEE J. Quant. Electron.* **1995**, *31*, 2241–2249.

(12) Noack, J.; Vogel, A. Laser-Induced Plasma Formation in Water at Nanosecond to Femtosecond Time Scales: Calculation of Thresholds, Absorption Coefficients, and Energy Density. *IEEE J. Quant. Electron.* **1999**, *35*, 1156–1167.

(13) Liu, W.; Kosareva, O.; Golubtsov, I.; Iwasaki, A.; Becker, A.; Kandidov, V.; Chin, S. Femtosecond Laser Pulse Filamentation Versus Optical Breakdown in H_2O. *Appl. Phys. B* **2003**, *76*, 215–229.

(14) Bergé, L.; Skupin, S.; Nuter, R.; Kasparian, J.; Wolf, J.-P. Ultrashort Filaments of Light in Weakly Ionized, Optically Transparent Media. *Prog. Rep. Phys.* **2007**, *70*, 1633.

(15) Liu, W.; Petit, S.; Becker, A.; Aközbek, N.; Bowden, C.; Chin, S. Intensity Clamping of a Femtosecond Laser Pulse in Condensed Matter. *Opt. Commun.* **2002**, *202*, 189 – 197.

(16) Zhao, C.; Qu, S.; Qiu, J.; Zhu, C. Photoinduced Formation of Colloidal Au by a Near-Infrared Femtosecond Laser. *J. Mater. Res.* **2003**, *18*, 1710–1714.

(17) Nakamura, T.; Mochidzuki, Y.; Sato, S. Fabrication of Gold Nanoparticles in Intense

Optical Field by Femtosecond Laser Irradiation of Aqueous Solution. *J. Mater. Res.* **2008**, *23*, 968–974.

(18) Herbani, Y.; Nakamura, T.; Sato, S. Synthesis of Platinum-Based Binary and Ternary Alloy Nanoparticles in an Intense Laser Field. *J. Colloid Interface Sci.* **2012**, *375*, 78 – 87.

(19) Sarker, M. S. I.; Nakamura, T.; Herbani, Y.; Sato, S. Fabrication of Rh Based Solid-Solution Bimetallic Alloy Nanoparticles with Fully-Tunable Composition Through Femtosecond Laser Irradiation in Aqueous Solution. *Appl. Phys. A* **2012**, *110*, 145–152.

(20) Nakamura, T.; Herbani, Y.; Ursescu, D.; Banici, R.; Dabu, R. V.; Sato, S. Spectroscopic Study of Gold Nanoparticle Formation Through High Intensity Laser Irradiation of Solution. *AIP Adv.* **2013**, *3*, 082101.

(21) Nakashima, N.; Yamanaka, K.; Saeki, M.; Ohba, H.; Taniguchi, S.; Yatsuhashi, T. Metal Ion Reductions by Femtosecond Laser Pulses with Micro-Joule Energy and Their Efficiencies. *J. Photochem. Photobiol. A* **2016**, *319–320*, 70 – 77.

(22) Tangeysh, B.; Moore Tibbetts, K.; Odhner, J. H.; Wayland, B. B.; Levis, R. J. Gold Nanoparticle Synthesis Using Spatially and Temporally Shaped Femtosecond Laser Pulses: Post-Irradiation Auto-Reduction of Aqueous [AuCl$_4$]$^-$. *J. Phys. Chem. C* **2013**, *117*, 18719–18727.

(23) Odhner, J. H.; Moore Tibbetts, K.; Tangeysh, B.; Wayland, B. B.; Levis, R. J. Mechanism of Improved Au Nanoparticle Size Distributions Using Simultaneous Spatial and Temporal Focusing for Femtosecond Laser Irradiation of Aqueous KAuCl$_4$. *J. Phys. Chem. C* **2014**, *118*, 23986–23995.

(24) Tangeysh, B.; Moore Tibbetts, K.; Odhner, J. H.; Wayland, B. B.; Levis, R. J. Triangular Gold Nanoplate Growth by Oriented Attachment of Au Seeds Generated by Strong Field Laser Reduction. *Nano Lett.* **2015**, *15*, 3377–3382.

(25) Tibbetts, K. M.; Tangeysh, B.; Odhner, J. H.; Levis, R. J. Elucidating Strong Field Photochemical Reduction Mechanisms of Aqueous $[AuCl_4]^-$: Kinetics of Multiphoton Photolysis and Radical-Mediated Reduction. *J. Phys. Chem. A* **2016**, *120*, 3562–3569.

(26) Tangeysh, B.; Tibbetts, K. M.; Odhner, J. H.; Wayland, B. B.; Levis, R. J. Gold Nanotriangle Formation Through Strong-Field Laser Processing of Aqueous $KAuCl_4$ and Postirradiation Reduction by Hydrogen Peroxide. *Langmuir* **2017**, *33*, 243–252.

(27) Belmouaddine, H.; Shi, M.; Karsenti, P.-L.; Meesat, R.; Sanche, L.; Houde, D. Dense Ionization and Subsequent Non-Homogeneous Radical-Mediated Chemistry of Femtosecond Laser-Induced Low Density Plasma in Aqueous Solutions: Synthesis of Colloidal Gold. *Phys. Chem. Chem. Phys.* **2017**, *19*, 7897–7909.

(28) Chin, S. L.; Lagacé, S. Generation of H_2, O_2, and H_2O_2 from Water by the Use of Intense Femtosecond Laser Pulses and the Possibility of Laser Sterilization. *Appl. Opt.* **1996**, *35*, 907–911.

(29) Besner, S.; Meunier, M. Femtosecond Laser Synthesis of AuAg Nanoalloys: Photoinduced Oxidation and Ions Release. *J. Phys. Chem. C* **2010**, *114*, 10403–10409.

(30) Oron, D.; Silberberg, Y. Spatiotemporal Coherent Control Using Shaped, Temporally Focused Pulses. *Opt. Express* **2005**, *13*, 9903–9908.

(31) Faccio, D.; Tamošauskas, G.; Rubino, E.; Darginavičius, J.; Papazoglou, D. G.; Tzortzakis, S.; Couairon, A.; Dubietis, A. Cavitation Dynamics and Directional Microbubble Ejection Induced by Intense Femtosecond Laser Pulses in Liquids. *Phys. Rev. E* **2012**, *86*, 036304.

(32) Finney, E. E.; Finke, R. G. Nanocluster Nucleation and Growth Kinetic and Mechanistic Studies: A Review Emphasizing Transition-Metal Nanoclusters. *J. Colloid Interface Sci.* **2008**, *317*, 351 – 374.

(33) Tatarchuk, V. V.; Sergievskaya, A. P.; Druzhinina, I. A.; Zaikovsky, V. I. Kinetics and Mechanism of the Growth of Gold Nanoparticles by Reduction of Tetrachloroauric Acid by Hydrazine in Triton N-42 Reverse Micelles. *J. Nanopart. Res.* **2011**, *13*, 4997–5007.

(34) Streszewski, B.; Jaworski, W.; Pacławski, K.; Csapó, E.; Dékány, I.; Fitzner, K. Gold Nanoparticles Formation in the Aqueous System of Gold(III) Chloride Complex Ions and Hydrazine Sulfate—Kinetic Studies. *Colloids Surf., A* **2012**, *397*, 63 – 72.

(35) Kane, D. J.; Trebino, R. Characterization of Arbitrary Femtosecond Pulses Using Frequency-Resolved Optical Gating. *IEEE J. Quant. Electron.* **1993**, *29*, 571–579.

(36) Sreeja, S.; Venugopal Rao, S.; Radhakrishnan, P.; Tewari, S. P.; Prem Kiran, P. Supercontinuum Emission from Water Using Femtosecond Pulses in the External Tight Focusing Limit. Proc. SPIE. 2012; pp 824718–824718–6.

(37) Sreeja, S.; Leela, C.; Kumar, V. R.; Bagchi, S.; Prashant, T. S.; Radhakrishnan, P.; Tewari, S. P.; Rao, S. V.; Kiran, P. P. Dynamics of Tightly Focused Femtosecond Laser Pulses in Water. *Laser Physics* **2013**, *23*, 106002.

(38) Milián, C.; Jarnac, A.; Brelet, Y.; Jukna, V.; Houard, A.; Mysyrowicz, A.; Couairon, A. Effect of Input Pulse Chirp on Nonlinear Energy Deposition and Plasma Excitation in Water. *J. Opt. Soc. Am. B* **2014**, *31*, 2829–2837.

(39) Eisenberg, G. Colorimetric Determination of Hydrogen Peroxide. *Ind. Eng. Chem., Anal. Ed.* **1943**, *15*, 327–328.

(40) Huckaba, C. E.; Keyes, F. G. The Accuracy of Estimation of Hydrogen Peroxide by Potassium Permanganate Titration. *J. Am. Chem. Soc.* **1948**, *70*, 1640–1644.

(41) McBride, R. S. The Standardization of Potassium Permanganate Solution by Sodium Oxalate. 1. *J. Am. Chem. Soc.* **1912**, *34*, 393–416.

(42) Keldysh, L. Ionization in Field of a Strong Electromagnetic Wave. *Sov. Phys. JETP* **1965**, *20*, 1307–1314.

(43) Fan, C.-H.; Longtin, J. P. Modeling Optical Breakdown in Dielectrics During Ultrafast Laser Processing. *Appl. Opt.* **2001**, *40*, 3124–3131.

(44) Fan, C. H.; Sun, J.; Longtin, J. P. Breakdown Threshold and Localized Electron Density in Water Induced by Ultrashort Laser Pulses. *J. Appl. Phys.* **2002**, *91*, 2530–2536.

(45) Efimenko, E. S.; Malkov, Y. A.; Murzanev, A. A.; Stepanov, A. N. Femtosecond Laser Pulse-Induced Breakdown of a Single Water Microdroplet. *J. Opt. Soc. Am. B* **2014**, *31*, 534–541.

(46) Sykora, S. Dawson Integral Approximations. DOI: 10.3247/SL4Soft12.001, 2012.

(47) Sarpe, C.; Köhler, J.; Winkler, T.; Wollenhaupt, M.; Baumert, T. Real-Time Observation of Transient Electron Density in Water Irradiated with Tailored Femtosecond Laser Pulses. *New J. Phys.* **2012**, *14*, 075021.

(48) Docchio, F. Lifetimes of Plasmas Induced in Liquids and Ocular Media by Single Nd:YAG Laser Pulses of Different Duration. *EPL (Europhysics Letters)* **1988**, *6*, 407.

(49) Crowell, R. A.; Bartels, D. M. Multiphoton Ionization of Liquid Water with 3.0 - 5.0 eV Photons. *J. Phys. Chem.* **1996**, *100*, 17940–17949.

(50) Pommeret, S.; Gobert, F.; Mostafavi, M.; Lampre, I.; Mialocq, J.-C. Femtochemistry of the Hydrated Electron at Decimolar Concentration. *J. Phys. Chem. A* **2001**, *105*, 11400–11406.

(51) Mao, S.; Quéré, F.; Guizard, S.; Mao, X.; Russo, R.; Petite, G.; Martin, P. Dynamics of Femtosecond Laser Interactions with Dielectrics. *Appl. Phys. A* **2004**, *79*, 1695–1709.

(52) LaMer, V. K.; Dinegar, R. H. Theory, Production and Mechanism of Formation of Monodispersed Hydrosols. *J. Am. Chem. Soc.* **1950**, *72*, 4847–4854.

(53) Xia, Y.; Xiong, Y.; Lim, B.; Skrabalak, S. Shape-Controlled Synthesis of Metal Nanocrystals: Simple Chemistry Meets Complex Physics? *Angew. Chem. Int. Ed.* **2009**, *48*, 60–103.

(54) Yan, H.; Cingarapu, S.; Klabunde, K. J.; Chakrabarti, A.; Sorensen, C. M. Nucleation of Gold Nanoparticle Superclusters from Solution. *Phys. Rev. Lett.* **2009**, *102*, 095501.

(55) Bastús, N. G.; Comenge, J.; Puntes, V. Kinetically Controlled Seeded Growth Synthesis of Citrate-Stabilized Gold Nanoparticles of up to 200 nm: Size Focusing versus Ostwald Ripening. *Langmuir* **2011**, *27*, 11098–11105.

(56) Watzky, M. A.; Finke, R. G. Transition Metal Nanocluster Formation Kinetic and Mechanistic Studies. A New Mechanism When Hydrogen is the Reductant: Slow, Continuous Nucleation and Fast Autocatalytic Surface Growth. *J. Am. Chem. Soc.* **1997**, *119*, 10382–10400.

(57) Shields, S. P.; Richards, V. N.; Buhro, W. E. Nucleation Control of Size and Dispersity in Aggregative Nanoparticle Growth. A Study of the Coarsening Kinetics of Thiolate-Capped Gold Nanocrystals. *Chem. Mater.* **2010**, *22*, 3212–3225.

(58) Njoki, P. N.; Luo, J.; Kamundi, M. M.; Lim, S.; Zhong, C.-J. Aggregative Growth in the Size-Controlled Growth of Monodispersed Gold Nanoparticles. *Langmuir* **2010**, *26*, 13622–13629.

(59) Zayats, M.; Baron, R.; Popov, I.; Willner, I. Biocatalytic Growth of Au Nanoparticles: From Mechanistic Aspects to Biosensors Design. *Nano Lett.* **2005**, *5*, 21–25.

(60) McGilvray, K. L.; Granger, J.; Correia, M.; Banks, J. T.; Scaiano, J. C. Opportunistic Use of Tetrachloroaurate Photolysis in the Generation of Reductive Species for the Production of Gold Nanostructures. *Phys. Chem. Chem. Phys.* **2011**, *13*, 11914–11918.

(61) McGilvray, K. L.; Fasciani, C.; Bueno-Alejo, C. J.; Schwartz-Narbonne, R.; Scaiano, J. C. Photochemical Strategies for the Seed-Mediated Growth of Gold and Gold–Silver Nanoparticles. *Langmuir* **2012**, *28*, 16148–16155.

(62) Haiss, W.; Thanh, N. T. K.; Aveyard, J.; Fernig, D. G. Determination of Size and Concentration of Gold Nanoparticles from UV–Vis Spectra. *Anal. Chem.* **2007**, *79*, 4215–4221.

(63) Kurihara, K.; Kizling, J.; Stenius, P.; Fendler, J. H. Laser and Pulse Radiolytically Induced Colloidal Gold Formation in Water and in Water-in-Oil Microemulsions. *J. Am. Chem. Soc.* **1983**, *105*, 2574–2579.

(64) Reuther, A.; Laubereau, A.; Nikogosyan, D. N. Primary Photochemical Processes in Water. *J. Phys. Chem.* **1996**, *100*, 16794–16800.

(65) Nikogosyan, D. N.; Oraevsky, A. A.; Rupasov, V. I. Two-Photon Ionization and Dissociation of Liquid Water by Powerful Laser UV Radiation. *Chem. Phys.* **1983**, *77*, 131 – 143.

(66) Behar, D.; Rabani, J. Kinetics of Hydrogen Production upon Reduction of Aqueous TiO$_2$ Nanoparticles Catalyzed by Pd$_0$, Pt$_0$, or Au$_0$ Coatings and an Unusual Hydrogen Abstraction; Steady State and Pulse Radiolysis Study. *J. Phys. Chem. B* **2006**, *110*, 8750–8755.

Graphical TOC Entry